

The CH₄ structure in Titan's upper atmosphere revisited

J. Cui,¹ R. V. Yelle,² D. F. Strobel,³ I. C. F. Müller-Wodarg,⁴ D. S. Snowden,²
T. T. Koskinen,² and M. Galand⁴

Received 26 July 2012; revised 18 September 2012; accepted 27 September 2012; published 15 November 2012.

[1] In this study, we reanalyze the CH₄ structure in Titan's upper atmosphere combining the Cassini Ion Neutral Mass Spectrometer (INMS) data from 32 flybys and incorporating several updates in the data reduction algorithms. We argue that based on our current knowledge of eddy mixing and neutral temperature, strong CH₄ escape must occur on Titan. Ignoring ionospheric chemistry, the optimal CH₄ loss rate is $\sim 3 \times 10^{27} \text{ s}^{-1}$ or 80 kg s^{-1} in a globally averaged sense, consistent with the early result of Yelle et al. (2008). The considerable variability in CH₄ structure among different flybys implies that CH₄ escape on Titan is more likely a sporadic rather than a steady process, with the CH₄ profiles from about half of the flybys showing evidence for strong escape and most of the other flybys consistent with diffusive equilibrium. CH₄ inflow is also occasionally required to interpret the data. Our analysis further reveals that strong CH₄ escape preferentially occurs on the nightside of Titan, in conflict with the expectations of any solar-driven model. In addition, there is an apparent tendency of elevated CH₄ escape with enhanced electron precipitation from the ambient plasma, but this is likely to be a coincidence as the time response of the CH₄ structure may not be fast enough to leave an observable effect during a Titan encounter.

Citation: Cui, J., R. V. Yelle, D. F. Strobel, I. C. F. Müller-Wodarg, D. S. Snowden, T. T. Koskinen, and M. Galand (2012), The CH₄ structure in Titan's upper atmosphere revisited, *J. Geophys. Res.*, 117, E11006, doi:10.1029/2012JE004222.

1. Introduction

[2] Among the major species in Titan's neutral upper atmosphere, CH₄ is the most elusive. The CH₄ density structure as measured by the Cassini Ion Neutral Mass Spectrometer (INMS) implies a large escape flux of $\sim 3 \times 10^9 \text{ cm}^{-2} \text{ s}^{-1}$ referred to the surface, or equivalently a loss rate of $\sim 2.5 \times 10^{27} \text{ s}^{-1}$, according to Yelle et al. [2008] (hereafter referred to as Y08). However, no convincing mechanism has been proposed so far that drives such a large CH₄ outflow. At the range of temperature in Titan's upper atmosphere ($\sim 110\text{--}190 \text{ K}$ [Westlake et al., 2011]), the thermal Jeans escape rate of $10^{13}\text{--}10^{20} \text{ s}^{-1}$ is far from sufficient. Strobel [2008, 2009] has argued that CH₄ loss from Titan is of hydrodynamic nature, but this was not confirmed by the Direct Simulation Monte Carlo (DSMC) results of Tucker and Johnson [2009] and Schaufelberger et al. [2012]. Current estimates of the nonthermal escape rates fall short by 2 orders

of magnitude [e.g., De La Haye et al., 2007]. Finally, Bell et al. [2010a] have proposed an alternative mechanism of aerosol trapping to interpret the CH₄ distribution with a negligible CH₄ escape rate, but later, Strobel [2012] has argued that this mechanism is operative well below the altitude range probed by the INMS and does not reduce the CH₄ escape rate significantly.

[3] The motivations for this study are twofold. First, there is still controversy on the interpretation of the INMS CH₄ data. The recent analysis of Bell et al. [2011] has obtained an optimal homopause level of $\sim 1000 \text{ km}$ on Titan and a typical CH₄ escape flux at least 2 orders of magnitude smaller than those of Y08 and Strobel [2008, 2009]. Since the early INMS works were published, the data from significantly more Titan flybys have now become available, and the data reduction algorithms have also been improved. These call for a reanalysis of the INMS CH₄ structure to solve the discrepancy between existing works. Second, the INMS investigations of the CH₄ structure so far primarily focus on the globally averaged situation. An analysis of the flyby-to-flyby variability is currently lacking and will be attempted here. This allows an assessment of the response of the CH₄ structure to varying solar and/or magnetospheric conditions.

[4] The organization of the paper is as follows. In section 2, we describe briefly the INMS sample included in this work, followed by a detailed description of the improvements in data reduction over previous works such as that by Müller-Wodarg et al. [2008] (hereafter referred to as MW08) and Cui et al. [2009] (hereafter referred to as C09). We present

¹School of Astronomy and Space Sciences, Nanjing University, Nanjing, China.

²Lunar and Planetary Laboratory, University of Arizona, Tucson, Arizona, USA.

³Department of Earth and Planetary Sciences, Johns Hopkins University, Baltimore, Maryland, USA.

⁴Department of Physics, Imperial College London, London, UK.

Corresponding author: J. Cui, School of Astronomy and Space Sciences, Nanjing University, Nanjing 210093, China. (jcui@nju.edu.cn)

©2012. American Geophysical Union. All Rights Reserved.
10.1029/2012JE004222

the main results of this paper in section 3, where several distinctive questions on the CH₄ structure in Titan's upper atmosphere are raised and their answers provided based on the reanalysis of the INMS data. Especially, we conclude that with the current knowledge of the eddy mixing profile and neutral temperature, strong CH₄ escape must occur on Titan. Finally, we give conclusions in section 4.

2. Data Reduction Algorithms

[5] The CH₄ densities in Titan's upper atmosphere have been extensively measured by the INMS during the Cassini encounters with Titan [Waite *et al.*, 2004]. Systematic analyses of the INMS CH₄ data have been presented in various works [e.g., Yelle *et al.*, 2006; Y08; MW08; C09; Magee *et al.*, 2009; Bell *et al.*, 2010a, 2011]. For this study, we combine the INMS neutral measurements from 32 Titan flybys, from T5 to T71. The data are obtained from the Planetary Plasma Interactions (PPI) node of the NASA Planetary Data System (PDS) public archives (<http://ppi.pds.nasa.gov>) and are reduced in a way similar to MW08 and C09. Nevertheless, several improvements in the INMS data reduction algorithms have been implemented in this study, which we detail in sections 2.1–2.3. A comparison with results from previous analyses is given in section 2.4.

2.1. Sensitivities and Wall Effects

[6] The conversion from the INMS raw count rates to number densities relies on the choice of the sensitivity values. For a given neutral species, the sensitivity values used for the data analysis are usually parameterized with a peak sensitivity and a cracking pattern (C09). Preliminary sensitivity values have been reported in C09, based on the calibrations made with either the flight unit (FU) or the refurbished engineering unit (REU) [see also Magee *et al.*, 2009]. Later, the REU sensitivities have been recalculated following updated REU calibration campaigns, but reporting peak values only (D. A. Gell *et al.*, Characterization of the Cassini Ion Neutral Mass Spectrometer (INMS): Revision of sensitivity values and implications for previous publications of INMS neutral densities and mixing ratios, manuscript in preparation, 2012, hereafter referred to as G12).

[7] Throughout this study, we adopt FU peak sensitivities and cracking patterns for all species with FU calibrations. For other species, we use the updated G12 peak sensitivities but still use the C09 cracking patterns. The updated REU calibrations do not necessarily affect the analysis of major neutral species such as N₂ and CH₄, since their sensitivities are based on FU calibration (C09). The situation for ⁴⁰Ar is more complicated, though the FU calibration results are used for this species. As illustrated in Y08, a proper determination of the ⁴⁰Ar densities requires a decoupling between ⁴⁰Ar and other minor species, especially CH₃C₂H. However, we will show below that in practice the decoupling depends on the CH₃C₂H cracking pattern rather than its peak sensitivity (see sections 2.3 for details). This means the updated REU calibrations do not affect the ⁴⁰Ar density determination as well. The ⁴⁰Ar density profile is critical for this study since as an inert and nonescaping species, it is useful for separating eddy mixing and molecular diffusion.

[8] An additional multiplicative factor, which is not implied by the updated REU calibrations, has to be adopted to account

for the difference in total density between INMS and other instruments. This factor is assumed to be common to all species, but its exact value is subject to uncertainty. A comparison between the INMS total densities and the Cassini Ultraviolet Imaging Spectrograph (UVIS) values for the T41 flyby suggests a multiplicative factor of 2.9 [Koskinen *et al.*, 2011], whereas a slightly lower value of 2.6 is inferred by matching the INMS total densities to the values from the Huygens Atmosphere Structure Instrument (HASI) and the Cassini Attitude and Articulation Control Subsystem (AACS) [Strobel, 2010]. A calibration factor of 2.9, common to all species, is adopted throughout this study (thus, all INMS peak sensitivities are divided by 2.9), but in practice, any value in the range of 2.6–3.2 is acceptable.

[9] Some portions of the INMS densities should be used with caution due to wall contamination, which primarily influences outbound densities but leaves inbound densities almost unaffected. Such an instrumental effect refers to adsorption/desorption or surface chemistry occurring on the INMS chamber walls [Vuitton *et al.*, 2008; C09]. Accordingly, throughout this study we focus on the N₂ and CH₄ densities from inbound only. For ⁴⁰Ar as a nonreactive species, wall contamination is not relevant, and both the inbound and outbound data are used.

2.2. Extraction of the N₂ and CH₄ Density Profiles

[10] For a given mass channel, the INMS records count rates in a primary counter (C1) as well as a low gain secondary counter (C2) [Waite *et al.*, 2004]. The latter is used only when the counts in the former are saturated. Due to dissociative ionization of neutral molecules by the INMS electron guns [Waite *et al.*, 2004], the density of a given species could be derived simultaneously from several channels. Specific strategies have to be designed to ensure that the densities from different channels are consistent and that the counts used are not affected by saturation [e.g., MW08; C09; Magee *et al.*, 2009].

[11] The N₂ and CH₄ densities are calculated following the scheme of MW08. In that work, the N₂ densities at most altitudes were obtained from C1 counts of either channel 28 or channel 14, depending on where C1 counts of channel 28 become saturated. Near the closest approach (CA) where C1 counts are saturated for both channels, C2 counts of channel 28 were used instead. The CH₄ densities were obtained from C1 counts of channel 16, but near CA where they become saturated, C1 counts of channel 12 were used. Channel 12 was chosen because it is not contaminated by ¹³CH₄.

[12] There are a few potential problems with the above approach. First, the transition level for the limit of saturation was set to where the count reaches 10⁵ per integration period (IP, 0.031 s) or 3.2 × 10⁶ s⁻¹ based on visual inspection of the INMS data from individual flybys, but a more careful inspection combining the data from all 32 flybys reveals that the C1 counter becomes saturated at a significantly lower level. However, this does not necessarily mean that the C1 count rates should be used in a more conservative manner. In contrast, we will show below that the transition level can in practice be extended to higher count rates by allowing for nonlinear conversion. Second, assuming a clear-cut transition between different channels usually leads to a rapid change in the characteristics of the INMS data at the specified transition levels, and consequently a discontinuity in the

derived N₂ or CH₄ density profile. This naturally introduces an artificial jump in the neutral temperature profile, which is derived from the density gradient. It will be shown below that these artificial density jumps can be largely removed by introducing continuously varying weighting functions for different channels. The improvements that we apply to the data reduction algorithms in this study are detailed as follows.

[13] First, we extend the transition levels to higher count rates by applying a correction for counter saturation in the region where the saturation is slight. An example is shown in Figure 1a where we plot the C1 count rate of channel 14, $C_1^{(14)}$, as a function of the C1 count rate of channel 28, $C_1^{(28)}$, both with dead time correction for detector fatigue [Magee *et al.*, 2009]. The INMS data from all 32 flybys have been included. The contributions of CH₄ and ¹⁴N¹⁵N to channel 14 have been subtracted, so both count rates in Figure 1a should measure the N₂ densities. For $C_1^{(28)} < 2 \times 10^6 \text{ s}^{-1}$, the two count rates are linearly correlated, suggesting that the C1 counters for both channels are not saturated and give reasonable measurements of the N₂ density. Above $\sim 2 \times 10^6 \text{ s}^{-1}$, $C_1^{(28)}$ curves up, indicative of counter saturation in channel 28. Up to $\sim (4-5) \times 10^6 \text{ s}^{-1}$, the relation between the two count rates can be described empirically by $C_1^{(14)} = a_0 C_1^{(28)} \exp \left\{ \tan \left[(a_1 C_1^{(28)})^{a_2} \right] \right\}$, with a_0 , a_1 and a_2 being free parameters to be constrained by the data. The C1 count rates of channel 28 corrected for saturation, $\hat{C}_1^{(28)}$, should satisfy $C_1^{(14)} = a_0 \hat{C}_1^{(28)}$ as long as $C_1^{(14)}$ is not saturated. Thus, we get

$$\hat{C}_1 = C_1 \exp \left\{ \tan \left[(a_1 C_1)^{a_2} \right] \right\}, \quad (1)$$

where we have dropped the superscript (28) because similar expressions are used to correct for the saturation of the C1 count rates of channels 14 and 16, as illustrated in Figures 1b and 1c, respectively.

[14] The free parameters, a_0 , a_1 and a_2 , are listed in Table 1 for reference. Note that a_0 is not used for correcting for saturation but instead used for ensuring that the densities derived from different channels and/or counters are consistent (see also section 2.4). These issues have been discussed in sections A3 and A1.2 of C09 in terms of the C1/C2 ratio and the calibration of the N₂/CH₄ cracking patterns. In previous analyses, the values for each of the above parameters were different from flyby to flyby, whereas in the present study, they are taken to be constant (see section 2.4 for details). The cutoff levels listed in Table 1 refer to the highest count rates for which equation (1) is applicable. Count rates above these cutoff levels are not used in our analysis. In practice, all C1 count rates of channel 16 can be safely used so that no cutoff level is given for this channel. By utilizing the count rates that are slightly saturated, the above procedure increases the signal-to-noise ratio of the density data near the transition regions as compared to early INMS analysis works.

[15] Second, the clear-cut transition at $4.2 \times 10^6 \text{ s}^{-1}$ from one channel to another (see Table 1) may cause density discontinuities in the derived N₂ profiles. To remove such features, the N₂ densities are calculated with

$W_1^{(28)}(z)N_1^{(28)}(z) + W_1^{(14)}N_1^{(14)}(z) + W_2^{(28)}N_2^{(28)}$ where $N_1^{(28)}(z)$, $N_1^{(14)}(z)$ and $N_2^{(28)}$ represent N₂ densities from C1 of channel 28, C1 of channel 14 and C2 of channel 28, respectively, $W_1^{(28)}$, $W_2^{(28)}$ and $W_1^{(14)}$ are predefined weighting functions constructed from hyperbolic tangents

$$W_1^{(28)}(t) = 1 - \frac{1}{2} \tanh \left[\frac{t - t_i^{(28)}}{\Delta t} \right] + \frac{1}{2} \tanh \left[\frac{t - t_o^{(28)}}{\Delta t} \right], \quad (2)$$

$$W_2^{(28)}(t) = \frac{1}{2} \tanh \left[\frac{t - t_i^{(14)}}{\Delta t} \right] - \frac{1}{2} \tanh \left[\frac{t - t_o^{(14)}}{\Delta t} \right], \quad (3)$$

$$W_1^{(14)}(t) = 1 - W_1^{(28)} - W_2^{(28)}. \quad (4)$$

In equations (2)–(4), t is time from CA, $t_i^{(28)}$ ($t_i^{(14)}$) and $t_o^{(28)}$ ($t_o^{(14)}$) correspond to where $C_1^{(28)}$ ($C_1^{(14)}$) reaches $4.2 \times 10^6 \text{ s}^{-1}$ during the inbound and outbound portions of a given flyby, and Δt is the timescale for the transition taken to be 10 s in this work. An example of these weighting functions is given in Figure 1d, assuming $t_i^{(28)} = -225 \text{ s}$, $t_o^{(28)} = +225 \text{ s}$, $t_i^{(14)} = -100 \text{ s}$ and $t_o^{(14)} = +100 \text{ s}$. The choice of the timescale for the transition, Δt , is not unique. Several values have been tested, but give identical N₂ density profiles.

[16] Finally, we note that the sampling of the INMS data is nonuniform. The data points from an individual flyby are often grouped in batches covering a very small time interval but with sequential groups separated by a much larger gap. Therefore as a third improvement, we average together all data points obtained within 1.5 s of each other, since they are expected to sample essentially the same portion of Titan's atmosphere. With a typical spacecraft velocity of 6 km s^{-1} , this time interval covers a length scale of $\sim 9 \text{ km}$ along the spacecraft trajectory. In practice, the procedure described above replaces each tightly packed group with a single data point with higher precision.

2.3. Extraction of the ⁴⁰Ar Density Profile

[17] As an inert and nonescaping species, the density profile of ⁴⁰Ar is unique for constraining the eddy mixing coefficients on Titan, which can then be used to infer the CH₄ escape flux [e.g., Y08; Bell *et al.*, 2011]. The ⁴⁰Ar atoms produce peak signals at mass channel 40, but the counts in this channel are also contributed significantly by CH₃C₂H. To illustrate the necessity of decoupling their cracking patterns, an example is provided in Figure 2 for the T18 flyby. We show with the solid circles the total count rate in channel 40 as a function of time from CA. The contributions from ⁴⁰Ar and CH₃C₂H are given separately by different symbols. The algorithm used for estimating these contributions is based on our nominal choice, which is explained in detail below. Figure 2 shows that without a proper decoupling, the outbound ⁴⁰Ar densities would be overestimated by a factor of ~ 2 .

[18] There are several complexities. First, the CH₃C₂H densities are usually obtained from counts in channels 37–39, but these channels are also contributed by C₆H₆ and

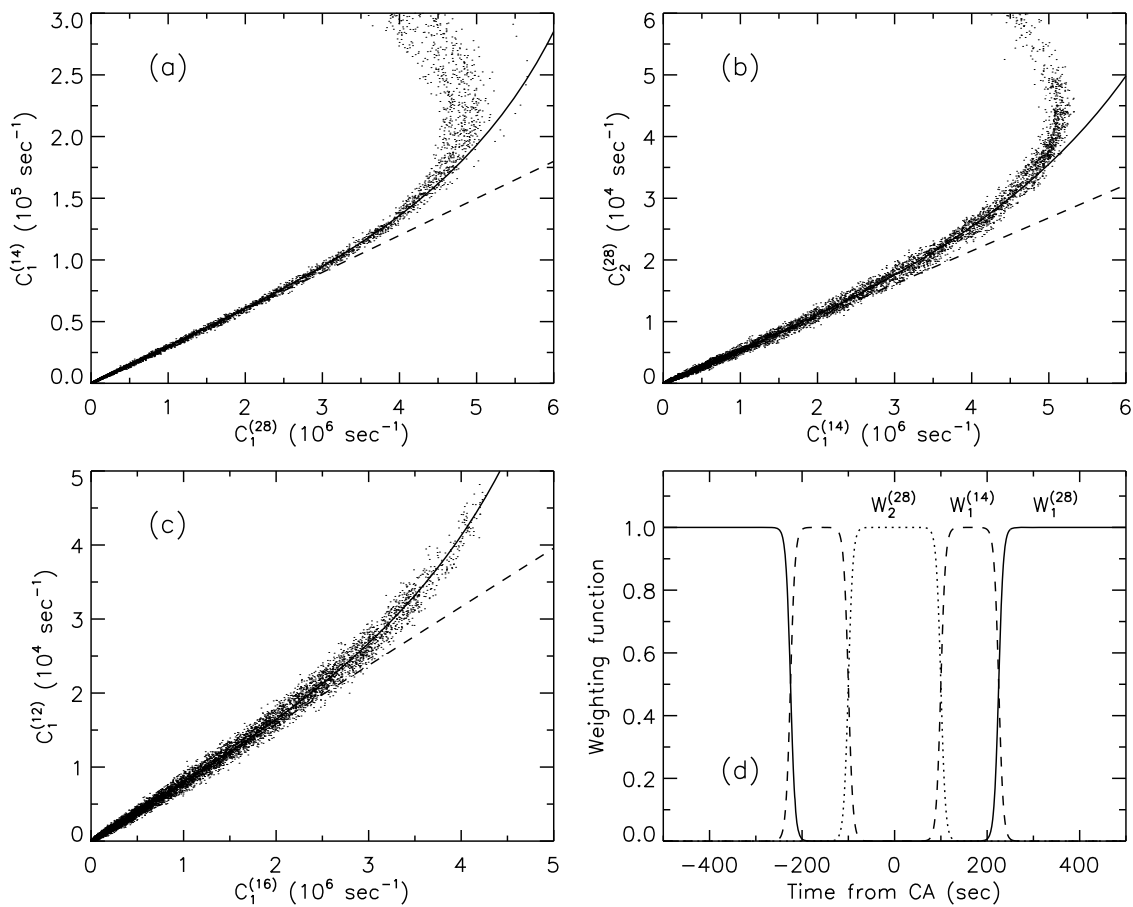


Figure 1. (a) The C1 count rate of channel 14 ($C_1^{(14)}$) as a function of the C1 count rate of channel 28 ($C_1^{(28)}$), both contributed by N₂ only. (b) The C2 count rate of channel 28 ($C_2^{(28)}$) as a function of the C1 count rate of channel 14 ($C_1^{(14)}$), both contributed by N₂ only. (c) The C1 count rate of channel 12 ($C_1^{(12)}$) as a function of the C1 count rate of channel 16 ($C_1^{(16)}$), both contributed by CH₄ only. The INMS data from all 32 flybys have been included. In Figures 1a–1c, the dashed line gives the linear correlation obtained from regions where both count rates are not saturated, and the solid line represents the nonlinear empirical relation used to correct for saturation up to the cutoff level given in Table 1. (d) The weighting functions for count rates in C1 of channel 28 ($W_1^{(28)}$, solid), C2 of channel 28 ($W_2^{(28)}$, dotted) and C1 of channel 14 ($W_1^{(14)}$, dashed), as a function of time from CA. These weighting functions are used for calculating the N₂ densities without instantaneous transition near the cutoff levels.

CH₃CN (C09). Their densities can be determined from counts in channels 77–78 and 41, respectively. Second, another relevant species is C₃H₆ that has not been included in our previous works. This can be seen from Figure 3 of C09, showing that the singular value decomposition (SVD) analysis has underpredicted the count rate in mass channel

42, the main peak of the C₃H₆ cracking pattern. Finally, it is also important that the contributions from background signals are subtracted before the count rates are converted to densities [C09; Magee *et al.*, 2009]. The background counts are estimated in a way similar to C09.

Table 1. Empirical Relations Between the Count Rates From Two Different Channels/Counters but Associated With the Same Ambient Species (N₂ or CH₄)^a

Species	Empirical Relation	a_0	a_1	a_2	Cutoff Level
N ₂	$C_1^{(14)} = a_0 C_1^{(28)} \exp\left\{\tan\left[\left(a_1 C_1^{(28)}\right)^{a_2}\right]\right\}$	0.0300	$1.27 \times 10^{-7} \text{ s}$	3.05	$4.2 \times 10^6 \text{ s}^{-1}$
N ₂	$C_2^{(28)} = a_0 C_1^{(14)} \exp\left\{\tan\left[\left(a_1 C_1^{(14)}\right)^{a_2}\right]\right\}$	0.00536	$1.12 \times 10^{-7} \text{ s}$	2.23	$4.2 \times 10^6 \text{ s}^{-1}$
CH ₄	$C_1^{(12)} = a_0 C_1^{(16)} \exp\left\{\tan\left[\left(a_1 C_1^{(16)}\right)^{a_2}\right]\right\}$	0.00791	$1.54 \times 10^{-7} \text{ s}$	2.77	N/A

^aAlso shown are the free parameters in these relations. Specifically, a_1 and a_2 are used to correct for saturations, whereas a_0 is used to ensure that the densities from different channels/counters are consistent. The cutoff level refers to the highest count rate for which the empirical expression is applicable. N/A, not available.

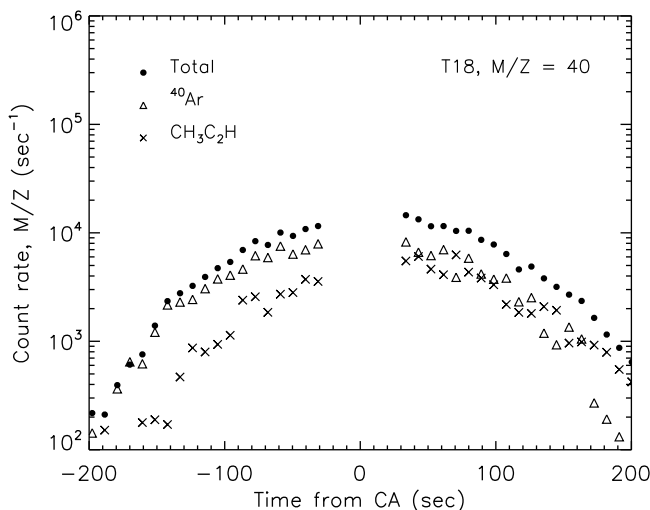


Figure 2. The count rate in mass channel 40 as a function of time from CA for the T18 flyby. Different symbols stand for the total count rates, the count rates contributed by ⁴⁰Ar and CH₃C₂H, respectively. The relative contributions of different species are calculated with the nominal algorithm (see text for details). The apparent asymmetry in CH₃C₂H is an indication of the wall chemistry effect.

[19] Among the neutral species mentioned above, CH₃C₂H and C₆H₆ have not been calibrated preflight. The updated REU calibration has inferred their peak sensitivities $\sim 30\%$ lower than the C09 values. For C₃H₆, neither FU nor REU calibration is available, leading to considerable uncertainty in evaluating its contributions to channels 37–39. Using the cracking pattern from the chemistry reference data of the National Institute of Standards and Technology (NIST, <http://webbook.nist.gov/chemistry/>) suggests that the C₃H₆ contribution to channel 39 is relatively small as compared to the other two channels. Therefore for our nominal choice, we derive the CH₃C₂H densities based on counts in channel 39 only, to minimize the uncertainty in the C₃H₆ cracking pattern. Especially, we notice that the CH₃C₂H densities from channels 37 and 38 are sometimes negative even near CA, implying that the NIST sensitivities of C₃H₆ for these two channels are probably higher than those appropriate to the INMS.

[20] We compare in Table 2 the ⁴⁰Ar number densities derived with several different algorithms. For each case, we combine the data from all 32 flybys in our sample, and the results for three different altitude ranges are presented. The first case corresponds to our nominal choice, i.e., with C₃H₆, C₆H₆ and CH₃CN included, with background subtracted, and with CH₃C₂H densities from channel 39 only.

Alternative algorithms in Table 2 include the case without background subtraction, the case without C₃H₆, the case without both C₃H₆ and C₆H₆, the case without CH₃CN, and the case with CH₃C₂H densities calculated as the average results of channels 37–39. The other aspects of these alternative algorithms remain the same as the nominal case.

[21] As compared to the nominal algorithm, the ⁴⁰Ar densities are overestimated by $\sim 5\%$ – 10% if the background counts are not subtracted, underestimated by $\sim 6\%$ if C₃H₆ is not included, and underestimated by nearly $\sim 15\%$ if neither C₃H₆ nor C₆H₆ is included. We emphasize that we consider C₃H₆ and C₆H₆ in our nominal analysis not because their direct contributions to channel 40 counts are significant. Instead, they are included to calculate more accurately the CH₃C₂H densities, thus representing an indirect influence to the ⁴⁰Ar density extraction as illustrated in Figure 2. Table 2 also shows that ignoring CH₃CN does not make any appreciable change to the derived ⁴⁰Ar densities. Finally, different channels used for determining the CH₃C₂H densities may lead to an uncertainty in ⁴⁰Ar at the level of $\sim 5\%$ – 10% .

[22] As mentioned in section 2.1, ⁴⁰Ar is a chemically inert species and not contaminated by any wall chemistry effect. This implies that the globally averaged inbound and outbound density profiles of ⁴⁰Ar should be roughly identical as long as the sample is sufficiently large [e.g., C09]. This fact could be used to evaluate a specific ⁴⁰Ar extraction algorithm since any imperfect decoupling of ⁴⁰Ar from other species, all of which are subject to wall contamination, may lead to an ⁴⁰Ar asymmetry between inbound and outbound. Several examples are given in Figure 3. For our nominal choice, the symmetry between inbound and outbound is maintained at all altitudes. This is also true for the case without background subtraction but more likely because the background signals are themselves symmetric about CA [see C09, Figures 33 and 34]. In contrast, there are clear differences between the inbound and outbound ⁴⁰Ar densities for the case without C₃H₆ and C₆H₆ included, as well as the case with CH₃C₂H densities from the averages of channels 37–39. The above comparison justifies, though indirectly, our nominal choice of the ⁴⁰Ar extraction algorithm in this study.

2.4. Comparisons With Previous Results

[23] We present in this section a comparison between the N₂, CH₄ and ⁴⁰Ar densities obtained here and those from previous works [e.g., MW08; C09] multiplied by the additional calibration factor of 2.9 (see section 2.1).

[24] In the N₂/CH₄ data reduction algorithms described in section 2.2, we have adopted a correcting function that varies for different channels (see Table 1). In contrast, it has been assumed in our previous analysis (C09; Y08; MW08)

Table 2. The ⁴⁰Ar Number Densities Calculated From Different Algorithms (See Text for Details) and Averaged Over Several Selected Altitude Bins Including All Flybys in Our Sample

Algorithm	960–980 km (cm ⁻³)	980–1000 km (cm ⁻³)	1000–1100 km (cm ⁻³)
Nominal	3.5×10^5	2.4×10^5	1.0×10^5
No background subtraction	3.8×10^5	2.6×10^5	1.1×10^5
No C ₃ H ₆	3.3×10^5	2.3×10^5	9.5×10^4
No C ₃ H ₆ and C ₆ H ₆	3.0×10^5	2.0×10^5	8.8×10^4
No CH ₃ CN	3.5×10^5	2.5×10^5	1.1×10^5
CH ₃ C ₂ H from mean of channels 37–39	3.8×10^5	2.5×10^5	9.7×10^4

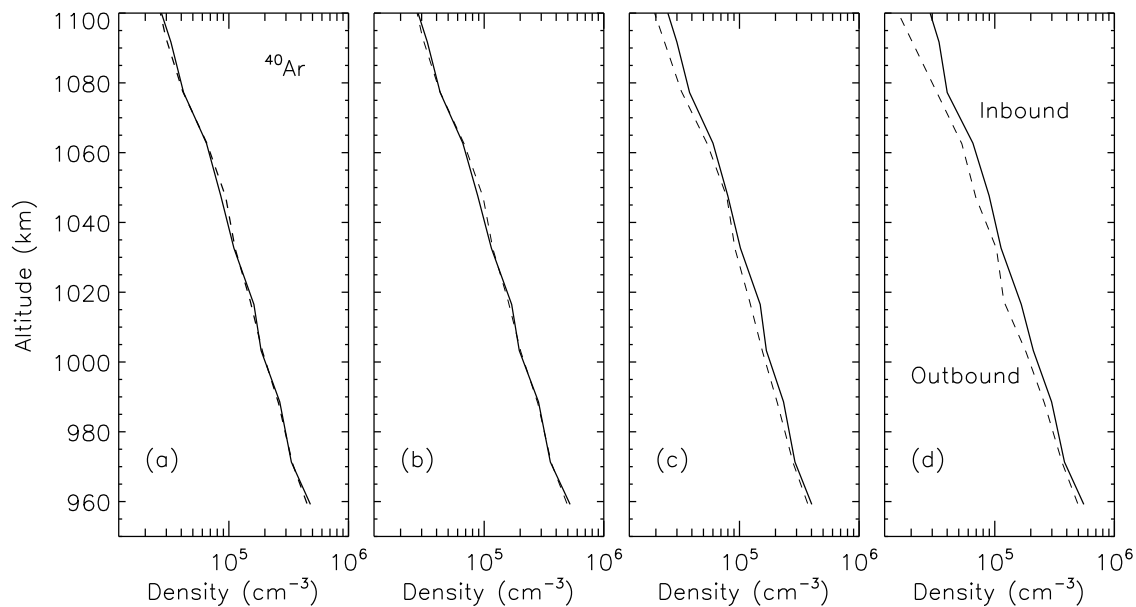


Figure 3. A comparison between the globally averaged inbound (solid) and outbound (dashed) density profiles of ^{40}Ar , obtained from several algorithms including (a) the nominal case, (b) the case without background subtraction, (c) the case without both C_3H_6 and C_6H_6 , and (d) the case with $\text{CH}_3\text{C}_2\text{H}$ densities from the averages of channels 37–39. For a reasonable scheme of ^{40}Ar density extraction, an asymmetry between the inbound and outbound profiles is not expected as ^{40}Ar is an inert species and is free from any wall chemistry effect.

that the saturation is due to the overload of the INMS detector system and thus the saturation characteristics are species independent. The early assumptions are incorrect as revealed by Figure 4, where we show the C2 count rates as a function of the C1 count rates for different channels. The data points from all 32 flybys have been included. The C1–C2 relations for channels 15 and 16, which are primarily contributed by CH_4 , are nearly identical and both are indicated by blue in Figure 4. Another group of relations, black for channel 14, red for channel 28 and green for channel 29, all of which are primarily contributed by N_2 or $^{14}\text{N}^{15}\text{N}$, is different from the relations for CH_4 . This strongly suggests that saturation is species dependent, though a rigorous interpretation based on physical arguments is currently lacking.

[25] When compared with MW08 and C09, the improvements in data reduction adopted here do not significantly alter the N_2 and CH_4 densities in regions where the C1 counts of channels 28 and 16 are not saturated, but the density differences in the saturated regions are not negligible. If we considered the T16 flyby (on 22 July 2006) as an example, we find that the N_2 densities reported here are $\sim 3\%$ – 5% higher than C09 near CA, and the CH_4 densities are higher by $\sim 15\%$ – 20% . These differences could be explained with the following arguments: The a_0 's parameters in Table 1 are related to the C1/C2 ratio and the calibration factors of channels 14 and 12 (C09). The latter were introduced in C09 to ensure that the N_2 and CH_4 densities from different channels are consistent. It is easily verified that the C1/C2 ratio is identical to the inverse of the multiplication of a_0 's for channels 28 and 14, which is ~ 6219 based on Table 1. The same ratio has been derived in our previous works as ~ 5976 for T16. The lower C1/C2 ratio in previous works, due to an overestimated saturation level, accounts for the N_2 density

difference reported above. Similarly, the CH_4 calibration factor for channel 12 is identical to the inverse of the multiplication of a_0 for channel 16 in Table 1 and 0.00636, the ratio of the channel 12 to channel 16 sensitivities for CH_4 . This factor is ~ 0.683 for T16 from our previous analysis and ~ 0.804 here which is common to all flybys. The difference of $\sim 18\%$ for this calibration factor is responsible for the CH_4 density difference between this work and C09.

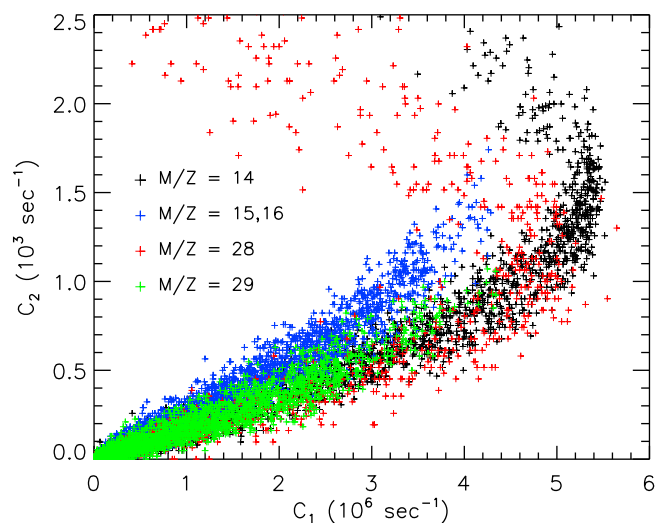


Figure 4. The C2 count rates as a function of the C1 count rates, for channels 14, 15, 16, 28 and 29. The data points from all flybys in our sample have been included. The C1–C2 relations indicate that the saturation characteristics are species dependent.

[26] The underestimates of the C09 and MW08 N₂ densities at relatively low altitudes are primarily associated with the early choice of the transition level ($3.2 \times 10^6 \text{ s}^{-1}$), which was based on an investigation of the $C_1^{(28)} - C_1^{(14)}$ relation for any given flyby. In practice, when including the data from only one flyby, the relatively large scattering of the $C_1^{(28)} - C_1^{(14)}$ relation makes it uncertain to characterize counter saturation, especially based on visual inspection. The impropriety of the early choice of the transition level is clearly revealed by Figure 1a, which indicates that the $C_1^{(28)} - C_1^{(14)}$ relation shows noticeable deviation from linearity for $C_1^{(28)} < 3.2 \times 10^6 \text{ s}^{-1}$. In this work, it is the combination of the data from all flybys that helps to constrain better the saturation characteristics. The underestimates of the C09 and MW08 CH₄ densities at low altitudes can be explained in a similar way. It is also worth emphasizing that the definition of the transition level here is different from that in previous works. In C09 and MW08, the transition level refers to where saturation occurs. In contrast, the definition of the transition level in this work is based on where the nonlinear relation, as described in section 2.2, starts to deviate from the data points. In both cases, the transition level corresponds to where the C1 counts can no longer be reliably used.

[27] As compared to the C09 results (multiplied by the calibration factor of 2.9), the ⁴⁰Ar densities reported here are generally decreased by $\sim 10\%$. The difference partly comes from the additional inclusion of C₃H₆ in this work. Also, the previous algorithms relied on a simultaneous fitting of counts in channels 37–39, whereas in this study we use channel 39 only, for the reason addressed in section 2.3. The recalibration of the REU sensitivities is not an issue since in both works the FU peak sensitivity is used for ⁴⁰Ar and the same cracking patterns are used for the other species involved, thus not changing their relative contributions to mass channel 40. To illustrate the update in ⁴⁰Ar density, we repeat our analysis on a sample identical to that of C09, i.e., up to T37, and we obtain at an altitude of 980 km an average ⁴⁰Ar density of $\sim 3.9 \times 10^5 \text{ cm}^{-3}$ for the nominal case and $\sim 4.2 \times 10^5 \text{ cm}^{-3}$ for the case without C₃H₆ and with CH₃C₂H densities from the average results of channels 37–39. The latter is identical to the value quoted by C09 when multiplied by 2.9.

[28] The INMS densities have also been calculated independently by Magee *et al.* [2009]. Their average values are $\sim 8.9 \times 10^9 \text{ cm}^{-3}$ for N₂, $\sim 2.0 \times 10^8 \text{ cm}^{-3}$ for CH₄ and $\sim 1.2 \times 10^5 \text{ cm}^{-3}$ for ⁴⁰Ar between 1000 and 1100 km when multiplied by 2.9. Taking into account the difference in peak sensitivities, the Magee *et al.* [2009] N₂, CH₄ and ⁴⁰Ar densities are about 15%, 10% and 20% lower than our nominal values obtained from an identical sample, i.e., from T18 to T43. The 1000–1100 km altitude range is typically where the C1 counts of channels 14 and 16 start to be saturated; thus, the difference in N₂ and CH₄ densities must be due to the respective methods used to correct for the saturation characteristics. The difference in ⁴⁰Ar densities cannot be traced back easily, as some of the details in their data reduction are not available to us. But we do note that for the algorithms listed in Table 2, the case without C₃H₆ and C₆H₆ reproduces the Magee *et al.* [2009] value most closely. It is

also noteworthy that despite of the 10–20% difference in absolute density, the ⁴⁰Ar mixing ratios from the two works are consistent.

[29] To end this section, we summarize the key issues of the updated N₂/CH₄/⁴⁰Ar data reduction algorithms: (1) comparisons with the total densities from other Cassini/Huygens instruments suggest that the absolute densities of all species have been underestimated by a factor of ~ 2.9 in previous analysis [e.g., C09; Y08; MW08; Cui *et al.*, 2008; Magee *et al.*, 2009]; (2) the N₂ and CH₄ densities near CA have been revised due to a more appropriate treatment of the saturation characteristics; (3) the instantaneous transitions in N₂ and CH₄ density profiles near regions where saturation occurs have been carefully removed in this study; and (4) the ⁴⁰Ar densities have been updated by including C₃H₆ in the decoupling and by restricting CH₃C₂H density extraction to channel 39 only.

[30] Finally, it should be remembered that the Cassini measurements of Titan's lower atmosphere have revealed seasonal variations [e.g., West *et al.*, 2011]; thus, the change in the globally averaged density profile of any species observed by the INMS is partly due to Titan's long-term thermospheric evolution over the time when the data were acquired. For example, with our updated data reduction algorithms and an averaging between 1000 and 1100 km, the N₂, CH₄ and ⁴⁰Ar densities drop by about 15%, 10% and 25% from the C09 sample (from 16 April 2005 to 19 November 2007) to the present sample including all available flybys (from 16 April 2005 to 7 July 2010).

3. Reanalysis of the CH₄ Structure in Titan's Upper Atmosphere

[31] Based on the improved reduction of the INMS data presented in section 2, several distinctive questions on the CH₄ structure in Titan's upper atmosphere are discussed below. In particular, our aim is to solve the discrepancy in the interpretation of the CH₄ data between existing works [e.g., Y08; Bell *et al.*, 2011].

[32] The mixing ratio profile of a minor species, *i*, in Titan's atmosphere is readily modeled with the one-dimensional, steady state diffusion equation:

$$F_i = -(D_i + K)n_a \frac{dX_i}{dr} - D_i n_a X_i \left(\frac{1}{H_i} - \frac{1}{H_a} + \frac{\alpha_i}{T} \frac{dT}{dr} \right), \quad (5)$$

to derive the eddy mixing coefficient and the diffusion flux (Y08). In equation (5), F_i , X_i , H_i , D_i , and α_i are the flux, mixing ratio, density scale height, and molecular diffusion coefficient of species *i*; n_a and H_a are the number density and density scale height of the background atmosphere; T is the neutral temperature; K is the eddy mixing coefficient; and r is the radial distance from Titan's center. In equation (5), we implicitly assume a common temperature profile for all atmospheric constituents.

[33] The results presented throughout this section are obtained within the framework of the fluid approach through equation (5), but we also note that the validity of such an approach has recently been questioned when compared to results from kinetic model calculations [e.g., Tucker and Johnson, 2009; Tucker *et al.*, 2012; Volkov *et al.*, 2011],

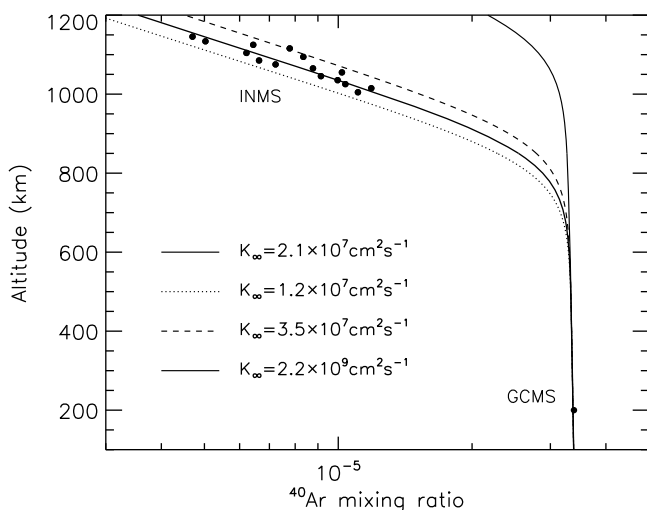


Figure 5. The diffusive equilibrium model fitting of the INMS and GCMS ^{40}Ar mixing ratios (solid circles) as a function of altitude throughout Titan's atmosphere. The INMS values are derived with the nominal choice of the ^{40}Ar data reduction algorithm (see section 2.3 for details). For illustrative purpose, the GCMS result is placed at 200 km, but the actual measurements were made at ~ 75 –140 km [Niemann *et al.*, 2010]. The best fit model is given by the solid line, with an asymptotic eddy mixing coefficient, $K_\infty \approx 2 \times 10^7 \text{ cm}^2 \text{ s}^{-1}$. Models with other choices of K_∞ are also indicated, including the case with $K_\infty \approx 2.2 \times 10^9 \text{ cm}^2 \text{ s}^{-1}$ that implies globally averaged CH_4 distribution under diffusive equilibrium.

especially in the transition region between strong collisional and collisionless.

3.1. How Important Is Eddy Mixing on Titan?

[34] It has been shown by Yelle *et al.* [2006, 2008] that the INMS CH_4 density profile can be interpreted by either the combination of diffusive equilibrium (i.e., $F_i = 0$) and an eddy mixing profile significantly larger than in any other solar system body or the combination of a large escape rate and an ordinary eddy mixing profile. To separate the above two effects, we first derive the eddy mixing coefficient as a function of altitude from the ^{40}Ar data.

[35] Eddy mixing in Titan's atmosphere is the summed effect of large-scale mixing by dynamics and small-scale mixing by turbulence [Müller-Wodarg and Yelle, 2002]. The former can only be obtained from time-dependent, full three-dimensional global circulation models [e.g., Müller-Wodarg *et al.*, 2000; Bell *et al.*, 2010b], and the latter is usually not resolved in these calculations. The analysis presented in this section is based on the steady state, one-dimensional calculations to be compared with the globally averaged ^{40}Ar data. This has the advantage of parameterizing the summed effect of all mixing processes, irrespective of the detailed mechanisms driving it.

[36] We adopt the empirical eddy mixing profile given by equation (4) of Y08, i.e., $K(z) = K_0(p_0/p)^\gamma K_\infty / [K_0(p_0/p)^\gamma + K_\infty]$, where p is atmospheric pressure, $p_0 = 1.43 \times 10^5 \text{ dyn cm}^{-2}$ (note the value of 1.43 dyn cm^{-2} given by Y08 is erroneous),

$K_0 = 3 \times 10^2 \text{ cm}^2 \text{ s}^{-1}$, $\gamma = 0.9$ and K_∞ is the asymptotic value of the eddy mixing coefficient. Such a functional form treats K_∞ as the only free parameter to be constrained by the data with a diffusive equilibrium model for ^{40}Ar . To constrain rigorously the eddy mixing profile, we combine the INMS ^{40}Ar data obtained above ~ 950 km and the tropospheric ^{40}Ar mixing ratio of $\sim 3.39 \times 10^{-5}$ measured by the Huygens Gas Chromatograph Mass Spectrometer (GCMS) below ~ 140 km [Niemann *et al.*, 2010].

[37] The interpolation of the ^{40}Ar mixing ratio profile to low altitudes using equation (5) requires a background model atmosphere to be constructed all the way from the top of the atmosphere down to the lower stratosphere. Several post-Cassini background models are available from the literature, including the model based on the HASI measurements made during the Huygens descending phase [Fulchignoni *et al.*, 2005], the model from Y08, and the standard chemical model of Strobel [2012]. These background models are denoted as HASI, RVY08, and DFS12, respectively. The HASI densities above 1000 km are systematically higher than the actual globally averaged values due to the oblateness of Titan's upper atmosphere (MW08), as the HASI data were acquired at the equatorial regions. The RVY08 model, which is based on previous INMS results, clearly underestimates the true atmospheric densities in the upper thermosphere by a factor of ~ 2.9 due to the uncertainty in absolute calibration (see section 2.1). The DFS12 model is the favored one for this study, as it is consistent with both the updated INMS total density profile and the range of Titan's average thermospheric temperature [e.g., C09; Westlake *et al.*, 2011].

[38] In Figure 5 we show the globally averaged INMS ^{40}Ar mixing ratio as a function of altitude. Such a profile is obtained by interpolating to a common altitude grid the observed ^{40}Ar mixing ratios based on the nominal data reduction algorithm described in section 2.3, which are then averaged over all flybys in our sample, both inbound and outbound. Also shown in Figure 5 is the best fit diffusive equilibrium model, with $K_\infty \approx 2 \times 10^7 \text{ cm}^2 \text{ s}^{-1}$, as well as models calculated with other choices of K_∞ . Especially, the dash-dotted line gives the model with $K_\infty \approx 2.2 \times 10^9 \text{ cm}^2 \text{ s}^{-1}$, required by the condition of CH_4 being in diffusive equilibrium (see below). This model shows considerable departure from the INMS data. For all cases, the background atmosphere is taken from the DFS12 standard chemical model, and the lower boundary condition is taken to

Table 3. Asymptotic Eddy Mixing Coefficient, K_∞ , and the CH_4 Homopause Level, $z_{\text{hom}}(\text{CH}_4)$, Calculated From Several Different Choices of the Background Model Atmosphere and the Input INMS ^{40}Ar Density Profile

Background Atmosphere	INMS ^{40}Ar Input	K_∞ ($\text{cm}^2 \text{ s}^{-1}$)	$z_{\text{hom}}(\text{CH}_4)$ (km)
DFS12	Nominal	2.0×10^7	855
	No $\text{C}_3\text{H}_6/\text{C}_6\text{H}_6$	1.6×10^7	845
	No background subtraction	2.2×10^7	860
RVY08	Nominal	5.0×10^7	875
	No $\text{C}_3\text{H}_6/\text{C}_6\text{H}_6$	4.1×10^7	865
	No background subtraction	5.5×10^7	880
HASI	Nominal	1.6×10^7	840
	No $\text{C}_3\text{H}_6/\text{C}_6\text{H}_6$	1.3×10^7	825
	No background subtraction	1.8×10^7	850

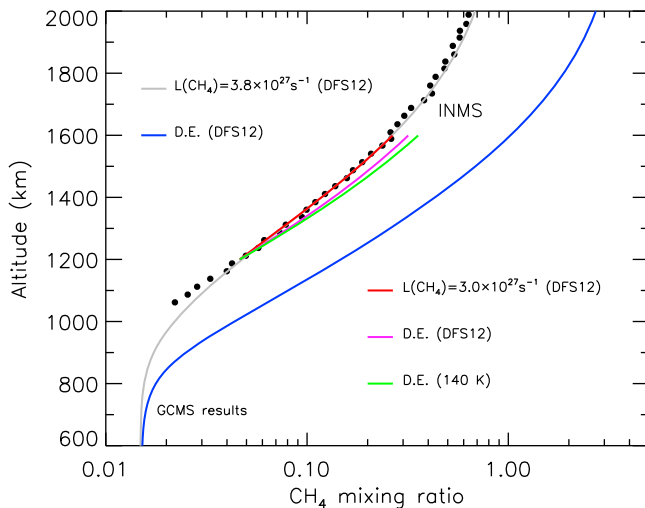


Figure 6. The CH₄ diffusion model profiles in Titan's upper atmosphere compared with the globally averaged INMS CH₄ densities from the updated data reduction algorithms. The density uncertainties due to counting statistics are too small to be visible at the scale shown. Five models are indicated, falling into two groups: (1) The gray and blue lines represent models calculated throughout the entire atmosphere and match the GCMS CH₄ mixing ratio of 1.48% deep in the lower stratosphere [Niemann *et al.*, 2010]. The former gives the best fit model with a loss rate of $3.8 \times 10^{27} \text{ s}^{-1}$ and the latter gives the diffusive equilibrium (DE) model. (2) The red, magenta and green lines represent models calculated in the 1200–1600 km altitude range, matching the INMS CH₄ mixing ratio of 4.6% at the lower boundary. The red line gives the best fit model with a loss rate of $3 \times 10^{27} \text{ s}^{-1}$, and the remaining two represent diffusive equilibrium models with different input background atmospheres (either DFS12 or isothermal at 140 K).

be consistent with the GCMS result [Niemann *et al.*, 2010]. Detailed in Table 3 are the K_{∞} values for several test runs with different choices of the background model atmosphere and different inputs of the INMS ⁴⁰Ar mixing ratio. These test runs give K_{∞} in the range of $\sim(1\text{--}6) \times 10^7 \text{ cm}^2 \text{ s}^{-1}$, comparable to the values in the upper atmospheres of other solar system bodies such as Mars [e.g., Rodrigo *et al.*, 1990] and Venus [e.g., von Zahn *et al.*, 1979]. For all cases the corresponding CH₄ homopause level is well below the 1000 km level suggested by Bell *et al.* [2011]. Our calculations indicate that above ~ 1200 km, the eddy mixing coefficient is at least 2 orders of magnitude lower than the molecular diffusion coefficient for CH₄. In section 3.2 we show that this has important impacts on the inference of CH₄ escape on Titan.

[39] Bell *et al.* [2011] used a simultaneous fitting to the ¹⁴N/¹⁵N and ⁴⁰Ar density data to constrain the eddy mixing profile, but we will not attempt this because the change in K_{∞} has a larger impact on the ⁴⁰Ar mixing ratio than on the ¹⁴N/¹⁵N mixing ratio, which makes ⁴⁰Ar a more sensitive diagnostic of eddy mixing. This could be seen from Bell *et al.* [2011, Figure 6], who show that enhanced eddy mixing leads to a factor of 2 increase in ⁴⁰Ar mixing ratio but only a 5% decrease in ¹⁴N/¹⁵N ratio at 1200 km.

[40] For further illustration, we use equation (5) to calculate the ¹⁴N/¹⁵N ratio as a function of altitude in Titan's upper atmosphere, with different choices of the temperature profile and eddy mixing coefficient. A fixed lower boundary condition of 167.7 is adopted, based on the updated GCMS result of Niemann *et al.* [2010]. For the DFS12 temperature profile and over the K_{∞} range of 1×10^7 to $1 \times 10^8 \text{ cm}^2 \text{ s}^{-1}$ (i.e., from 1/5 to 5 times the nominal value), we find a range in ¹⁴N/¹⁵N of $\sim 200\text{--}220$ at 1200 km. For the RVY08 and HASI temperature profiles, the corresponding ranges are $\sim 210\text{--}230$ and $\sim 190\text{--}210$, respectively. Thus, it is clear that ⁴⁰Ar is a more powerful and preferred constraint on eddy mixing as a combined result of (1) the uncertainty in temperature and (2) the insensitivity of ¹⁴N/¹⁵N ratio to K_{∞} .

3.2. Does Strong CH₄ Escape Occur on Titan?

[41] As soon as the eddy mixing profile is known, the CH₄ distribution is readily modeled with equation (5), treating the CH₄ escape rate as the only free parameter. For a preliminary test of the model validity, we show with the light solid line in Figure 6 the model profile obtained by integrating equation (5) upward from the lower stratosphere where the CH₄ mixing ratio is set as 1.48% based on the GCMS result [Niemann *et al.*, 2010]. A CH₄ loss rate, $L(\text{CH}_4)$, of $3.8 \times 10^{27} \text{ s}^{-1}$ is used for constructing the model. The neutral temperature profile is taken from the DFS12 background atmosphere, and $K_{\infty} \approx 2 \times 10^7 \text{ cm}^2 \text{ s}^{-1}$ is adopted for self-consistency (see Table 3). The model adequately reproduces the INMS CH₄ data in the 1200–1600 km altitude range but systematically overestimates the data both below and above.

[42] The departure below ~ 1200 km comes from the fact that the chemical destruction of CH₄ molecules has been ignored. In Titan's upper atmosphere, CH₄ photolysis typically peaks at ~ 850 km [Lavvas *et al.*, 2011], and the effects of magnetospheric destruction may vary considerably in response to the plasma environment [e.g., Rymer *et al.*, 2009]. Strobel [2009] has recently shown that the CH₄ loss rate derived from the INMS data may differ by $\sim 20\%$ with or without ionospheric chemistry included. It is also likely that the specific functional form of the eddy mixing profile adopted in this study has some impact on the model CH₄ mixing ratios below ~ 1200 km. We note that in the analysis of Y08, the lower boundary for CH model fitting is placed at ~ 950 km, which is the lowest altitude probed by the INMS. The choice of the lower boundary at 1200 km is in fact a quite significant difference between the two works. The present choice lessens the sensitivity of the model results to both CH₄ photochemical destruction and eddy mixing, whose influences tend to diminish with increasing altitude.

[43] Above ~ 1600 km, the Knudsen number, K_n , defined as the ratio between the particle mean free path and the atmospheric scale height, becomes sufficiently high that a kinetic model should be used instead [e.g., Volkov *et al.*, 2011]. Bird [1994] argued that the fluid description is only valid with $K_n < 0.2$, which corresponds to a typical altitude of ~ 1400 km for CH₄ on Titan. However, Figure 6 indicates that the diffusion model can in practice be extended upward by at least 200 km and still with satisfactory results.

[44] Based on the above discussions, we use the INMS CH₄ densities in the 1200–1600 km range for the data-model comparison to ensure that the effect of chemical destruction is negligible, that the exact form of the eddy mixing profile is not

Table 4. The Best Fit CH₄ Loss Rates for Different Input Parameters of the Asymptotic Eddy Mixing Coefficient, K_∞ , and Isothermal Neutral Temperature, T^a

Model	K_∞ (cm ² s ⁻¹)	T (K)	$L(\text{CH}_4)$ (s ⁻¹)
1	2×10^7	DFS12	3.0×10^{27}
2	2.2×10^9	DFS12	DE
3	2×10^7	140	4.5×10^{27}
4	2×10^7	150	2.7×10^{27}
5	2.6×10^9	145	DE
6	2×10^7	165	DE

^aDiffusive equilibrium (DE) is obtained for some extreme choices of the model input.

important, and that the fluid description is valid. The corresponding best fit CH₄ diffusion model is indicated by the red line in Figure 6, with a CH₄ loss rate of $\sim 3.0 \times 10^{27}$ s⁻¹ or a CH₄ upward flux of $\sim 3.6 \times 10^9$ cm⁻² s⁻¹ referred to the surface, in agreement with the early results of Y08 and Strobel [2008, 2009]. Here the DFS12 background atmosphere and a nominal eddy mixing coefficient of $K_\infty \approx 2 \times 10^7$ cm² s⁻¹ have been used. The CH₄ flux inferred above accounts for $\sim 65\%$ of the CH₄ limiting flux well below Titan's homopause.

[45] Table 4 lists the results from model runs with different input profiles of the eddy mixing coefficient and neutral temperature. All models are calculated with a fixed CH₄ mixing ratio of 4.6% at the lower boundary (1200 km), based on the updated INMS data reduction algorithms. For models 1–2, the temperature profile is taken from the DFS12 background atmosphere, whereas for the other models isothermal condition is assumed. The diffusive equilibrium solutions for several model inputs are illustrated in Figure 6 for comparison. The change in the best fit CH₄ loss rate with continuously varying eddy mixing coefficient, K_∞ , and isothermal temperature, T , is illustrated in Figure 7. Some extreme models are able to reproduce the INMS CH₄ data

without invoking a large CH₄ loss rate. If we restrict temperature in the 140–150 K range as implied by existing INMS analyses, the eddy mixing coefficient, K_∞ , has to be $\sim (2-3) \times 10^9$ cm² s⁻¹ to suppress the CH₄ loss rate below the typical nonthermal level [e.g., *De La Haye et al.*, 2007]. If we use K_∞ values consistent with the INMS and GCMS ⁴⁰Ar data, the neutral temperature has to be ~ 165 K to maintain CH₄ diffusive equilibrium. Occasionally the neutral temperature in Titan's upper atmosphere reaches such a high level [*Westlake et al.*, 2011], but this only occurs for particular flybys and cannot be used as the globally averaged value.

[46] We conclude that strong CH₄ escape does occur on Titan, with a globally averaged loss rate of $\sim 3 \times 10^{27}$ s⁻¹ which is many orders of magnitude higher than the Jeans rate. We reach this conclusion by combining our knowledge of (1) the ⁴⁰Ar structure throughout the entire atmosphere based on the INMS and GCMS data and (2) the CH₄ structure in the 1200–1600 km range based on the INMS data only. The inclusion of the GCMS ⁴⁰Ar data (obtained well below the homopause) is essential for constraining the eddy mixing profile since the INMS ⁴⁰Ar mixing ratio (obtained well above the homopause) is not sensitive to K_∞ when $K \ll D_i$. In contrast, we do not require that the CH₄ model profiles reproduce the GCMS CH₄ mixing ratio of 1.48% [*Niemann et al.*, 2010]. For example, the gray solid line in Figure 6, when extrapolated downward with equation (5), approaches asymptotically 1.25% in the lower stratosphere. We expect that the difference in the stratospheric CH₄ mixing ratio could be compensated for by including chemical destruction terms in the model calculations [*Strobel*, 2012].

3.3. How Variable Is CH₄ Escape on Titan?

[47] In this section, we investigate the variability of CH₄ escape and search for potential trends with solar and/or magnetospheric conditions. We derive for each flyby the best fit CH₄ loss rate with the one-dimensional, steady state

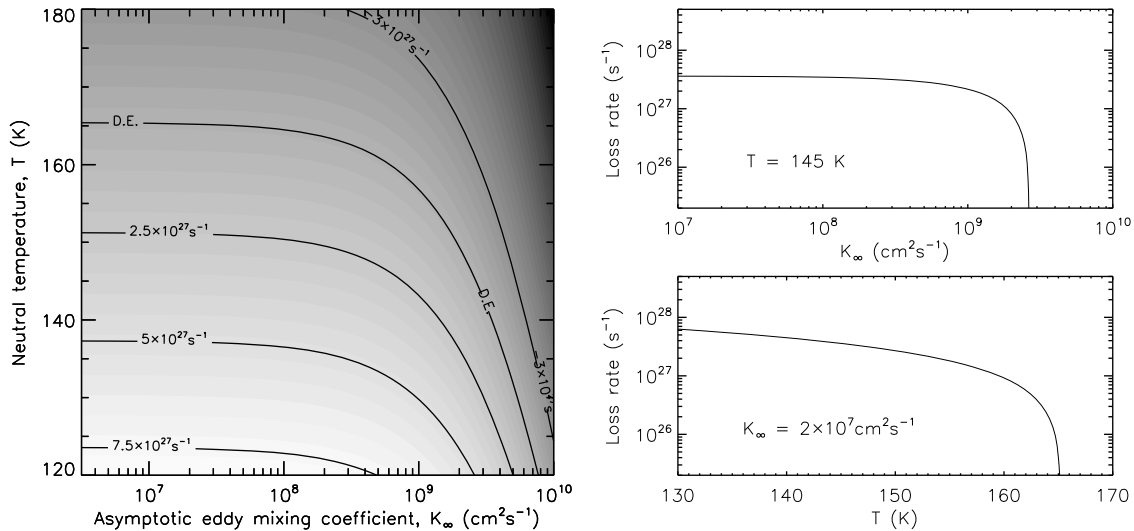


Figure 7. (left) The best fit CH₄ loss rate as a function of asymptotic eddy mixing coefficient, K_∞ , and isothermal neutral temperature, T . (top right) The variation of the CH₄ loss rate with K_∞ when T is fixed to 145 K (bottom right) the CH₄ loss rate with T when K_∞ is fixed to 2×10^7 cm² s⁻¹. The inference of strong CH₄ escape on Titan is based on the optimal range of these two parameters, as constrained by our current knowledge of the N₂ and ⁴⁰Ar density structures.

Table 5. The Best Fit CH₄ Loss Rate Calculated From the Diffusion Model Fitting to the Updated INMS CH₄ Data for Each Flyby in Our Sample^a

Flyby	Date (Earth Day)	LAT LON	SZA	LST	<i>T</i>	(K)	<i>L</i> (CH ₄) (10 ²⁷ s ⁻¹)	<i>e</i> 0.6 eV to 5 MeV	Ions 1 eV to 50 keV	<i>p</i> * 27–255 keV
T5	-1578	67°N	355°	108°	17:40	156 ± 2	3.8 ± 0.5	Plasma sheet	Plasma sheet	Medium
T18	-1053	75°N	111°	102°	06:50	121 ± 2	<1.9	Lobe-like	Lobe-like	High
T21	-973	60°N	229°	132°	22:41	157 ± 2	2.0 ± 0.5	Mixed	Mixed	High
T23	-941	52°N	20°	67°	12:34	147 ± 2	<1.2	Plasma sheet	Plasma sheet	Medium
T25	-901	5°N	25°	172°	23:58	171 ± 3	2.2 ± 0.3	Unidentified	Unidentified	Low
T26	-885	7°N	11°	166°	00:52	143 ± 2	2.4 ± 0.2	Bimodal	Heavy-riched	Medium
T28	-854	25°N	13°	164°	00:41	143 ± 2	<0.9	Mixed	Mixed	High
T29	-838	34°N	14°	157°	00:32	157 ± 3	2.0 ± 0.4	Plasma sheet	Plasma sheet	Medium
T30	-822	42°N	17°	150°	00:19	155 ± 2	2.5 ± 0.3	Mixed	Mixed	Medium
T32	-790	57°N	24°	135°	23:47	131 ± 2	<0.9	Magnetosheath	Magnetosheath	High
T36	-679	49°S	63°	93°	19:10	180 ± 4	2.9 ± 0.2	Plasma sheet	Plasma sheet	High
T39	-600	75°S	71°	83°	18:31	120 ± 3	<0.7	Plasma sheet	Plasma sheet	High
T40	-584	20°S	104°	63°	16:16	138 ± 2	1.2 ± 0.3	Bimodal	Heavily enriched	Medium
T42	-504	39°S	127°	46°	14:32	158 ± 2	1.5 ± 0.4	Magnetosheath	Magnetosheath	High
T43	-456	3°N	114°	50°	15:15	107 ± 3	<2.2	Lobe-like	Mixed	High/Medium
T50	-186	58°S	328°	120°	00:17	138 ± 3	-2.5 ± 0.8	Mixed	Mixed	High
T56	-67	7°S	164°	160°	22:47	122 ± 6	<1.6	Mixed	-	High
T57	-51	17°S	163°	155°	22:48	151 ± 5	4.1 ± 1.0	Mixed	-	High/Medium
T58	-35	27°S	162°	148°	22:48	149 ± 4	5.7 ± 0.7	Plasma sheet	-	Medium
T59	-19	36°S	161°	140°	22:52	141 ± 1	-1.2 ± 0.3	Mixed	-	Medium
T65	153	58°S	20°	112°	03:17	146 ± 2	<1.9	-	-	-
T71	329	44°S	341°	105°	04:58	140 ± 1	2.5 ± 0.3	-	-	-

^aAlso listed are the date of observation in units of Earth days before (indicated by negative) or after (indicated by positive) equinox (on 11 August 2009), latitude (LAT), longitude (LON), solar zenith angle (SZA), local solar time (LST), as well as the characteristics of the ambient plasma following the classification schemes of *Rymer et al.* [2009], *Németh et al.* [2011] and *Garnier et al.* [2010]. Heavy-riched means events enriched with heavy ions. The geophysical parameters are given for a reference altitude of 1400 km; *p** indicates energetic protons. The uncertainties of *T* and *L*(CH₄) as well as the upper limits for *L*(CH₄) are evaluated with a Monte Carlo approach which takes into account the effects of both counting statistics and density fluctuations due to wave structures.

diffusion model based on a common eddy mixing profile with $K_{\infty} \approx 2 \times 10^7 \text{ cm}^2 \text{ s}^{-1}$. Using different K_{∞} values gives very similar results as eddy mixing is unimportant at the altitudes involved in the model fitting. This is justified by Figure 7 (top right), which shows that over the range of possible K_{∞} values (several $10^7 \text{ cm}^2 \text{ s}^{-1}$), the impact of eddy mixing is small. The neutral temperature is obtained from the hydrostatic fitting to the N₂ densities for each flyby, assuming isothermal.

[48] More specifically, we evaluate the best fit temperature and CH₄ loss rate, as well as their uncertainties, with a Monte Carlo approach [e.g., *Pang*, 2006]. For a given flyby, we obtain the large-scale trends for N₂ and CH₄ in Titan's upper atmosphere based on the third-order polynomial fittings to the logarithmic N₂/CH₄ densities as a function of altitude. We then generate 1000 random realizations of the N₂ and CH₄ profiles of this flyby that encompass the apparent wiggles in the INMS data around the large-scale trends. This is accomplished by artificially placing random fluctuations around the polynomial fits with altitude dependent magnitudes equal to the measured density variations along the spacecraft trajectory. For each random realization, we apply isothermal fitting to N₂ and diffusion model fitting to CH₄. The averages (standard deviations) of the random temperature and loss rate values are then taken to be their respective best fit values (uncertainties). The wiggles in the data are contributed not only by counting statistics but also by gravity wave perturbations which are persistently seen in Titan's upper atmosphere [e.g., *Fulchignoni et al.*, 2005; *Müller-Wodarg et al.*, 2006; *Koskinen et al.*, 2011]. Variations due to counting statistics are $\sim(1-2)\%$ at a reference altitude of 1400 km (C09) and the wave amplitudes are

typically 10% of the mean densities [*Müller-Wodarg et al.*, 2006]. In practice, the uncertainty due to density wiggles is more important than that due to counting statistics and that due to finite temperature gradient. The latter justifies the isothermal assumption adopted throughout this section.

[49] The best fit CH₄ loss rates and neutral temperatures are detailed in Table 5. Nearly 1/3 flybys have been excluded either due to the insufficient coverage of the INMS data in the 1200–1600 km altitude range, or due to large variations of the INMS densities around the empirical trend that lead to significant uncertainties in the derived temperatures and loss rates. The former is primarily caused by INMS ram angles too large to allow accurate density determination, and the latter, as seen in the T37, T48 and T61 flybys, might be indicative of large amplitude wave structures in the ambient atmosphere. Since Table 5 only gives a portion of the available INMS sample, the average of the listed CH₄ loss rates is not exactly identical to the value of $3.0 \times 10^{27} \text{ s}^{-1}$ reported in section 3.2. Also note that the neutral temperatures listed in the table are not exactly equal to those of *Westlake et al.* [2011] due to different altitude ranges used for isothermal fitting.

[50] Several examples of the INMS CH₄ mixing ratio profiles are presented in Figure 8 between 1200 and 1600 km. The diffusive equilibrium models are indicated by the dashed lines for comparison. Figure 8 reveals a large variability in the pattern of CH₄ bulk flow. The T5, T29 and T71 plots correspond to cases with strong CH₄ outflow at the level of several 10^{27} s^{-1} . The T23 and T39 plots show cases with CH₄ distributions under approximate diffusive equilibrium. The inference of diffusive equilibrium for a specific flyby is made based on the criterion that the actual best fit flux is less than 3

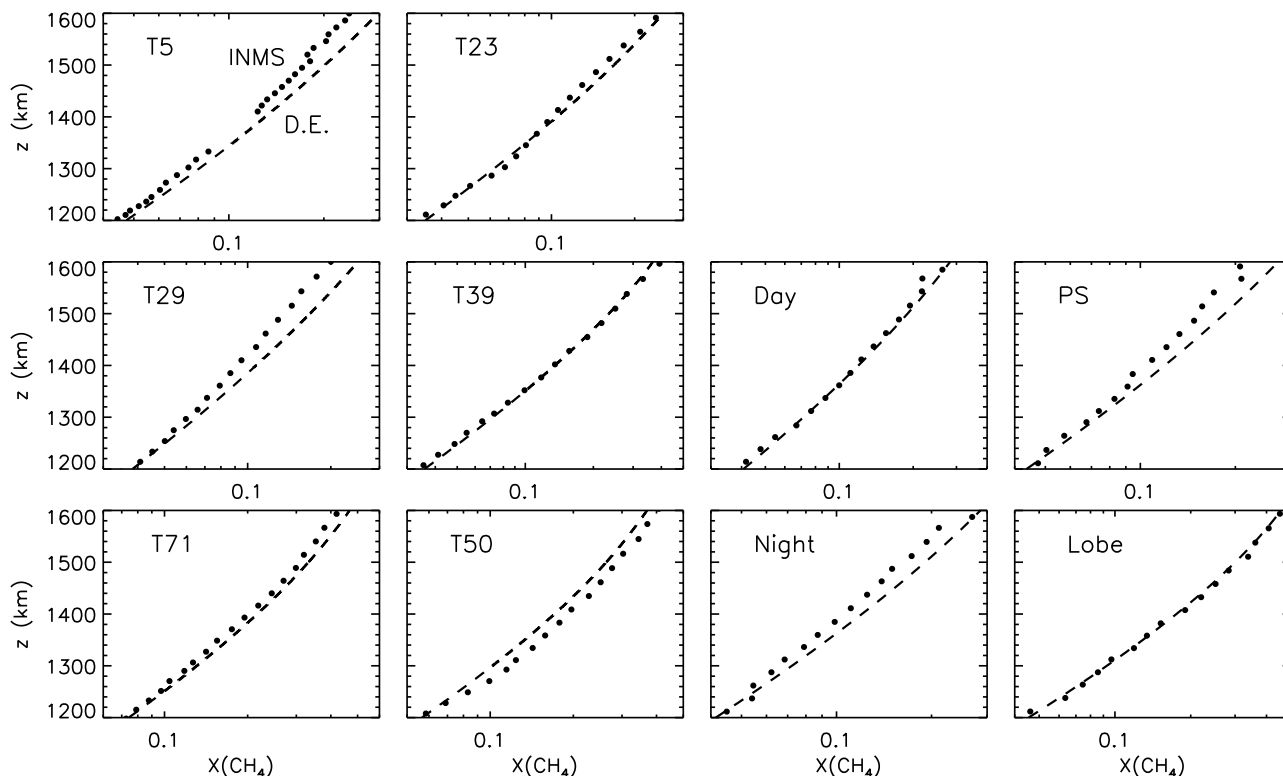


Figure 8. The INMS CH₄ mixing ratio profiles for several example flybys and categories with different solar and/or magnetospheric conditions. For comparison, the dashed line gives the diffusive equilibrium (DE) model. A considerable variability in CH₄ structure is revealed and suggests that CH₄ escape on Titan is more likely to be sporadic rather than steady. Specifically, cases with strong escape include T5, T29, T71, T50, the nightside (night) category and the plasma sheet (PS) category, whereas the data from T23, T39, the dayside (day) category and the lobe-like (lobe) category are reasonably described by diffusive equilibrium.

times the flux uncertainty. The T50 plot is an example with the best fit CH₄ flux being inward. Cases with CH₄ outflow are seen in 12 out of 22 flybys in our sample ($\sim 55\%$). The diffusive equilibrium cases are seen in eight flybys ($\sim 36\%$), and for each of them we provide in Table 5 the corresponding 3σ upper limit of the CH₄ outflow rate. Finally, cases with CH₄ inflow are seen in only two flybys. The variability of CH₄ bulk flow revealed by Table 5 is considerably larger than that for H₂, which remains roughly constant among different flybys [Cui *et al.*, 2011]. The INMS data used for this study have been acquired primarily under solar minimum conditions, with $\sim 10\%$ variance in solar activities based on either the F10.7 cm or 121.6 nm solar irradiance, as reported by the space weather prediction center of the National Oceanic and Atmospheric Administration (NOAA). Not surprisingly, it would be difficult to explain the variability of CH₄ bulk flow as solar-driven only.

[51] Table 5 also shows that the CH₄ flow in Titan's upper atmosphere is preferentially outward. If the flows from individual flybys were eventually associated with horizontal transport rather than escape [Tucker and Johnson, 2009], a considerable portion of the flybys with inward flow would be expected in our sample. But the INMS data do not support this. In the following we will interpret the CH₄ flux derived for any individual flyby as an escape flux, except for the two flybys with best fit CH₄ flux being negative. This means we

assume the true sinks of CH₄ molecules reside far away in the interplanetary space rather than some horizontally connected regions on Titan [see also Yelle *et al.*, 2006]. A rigorous evaluation of such an issue will be presented in a future paper (I. C. F. Müller-Wodarg *et al.*, The role of thermospheric winds on the distribution of CH₄ and ⁴⁰Ar in Titan's upper atmosphere, manuscript in preparation, 2012). It is also worth mentioning that the observed variability in CH₄ structure could be either spatial or temporal. If the latter is dominant, the variability reported here is not necessarily indicative of horizontal transport.

[52] One of the prominent features revealed by Table 5 is that strong CH₄ escape preferentially occurs on the nightside. We note that for the five flybys with dayside trajectories (defined here as $\text{SZA} < 90^\circ$ at a reference altitude of 1400 km), three (T23, T39 and T50) show CH₄ distributions under approximate diffusive equilibrium, and two of the remaining flybys (T40 and T42) are characterized by relatively small CH₄ loss rates of $\sim 1.2 \times 10^{27} \text{ s}^{-1}$ and $\sim 1.5 \times 10^{27} \text{ s}^{-1}$. In contrast, all the three flybys with the largest CH₄ escape rates ($> 3 \times 10^{27} \text{ s}^{-1}$) occur deep in the nightside. The above difference is clearly seen in Figure 8 (third column), where we compare the diffusive equilibrium distribution for CH₄ with the INMS profile averaged over all measurements made on the dayside or nightside. This is obviously in conflict with the expectations of any

Table 6. Mean CH₄ Loss Rates and Neutral Temperatures for Different Categories of Titan Flybys^a

Category	Neutral Temperature (K)	CH ₄ Loss Rate (s ⁻¹)	Flybys Included
Dayside	148	DE	T23, T40, T41, T42, T43, T48
Nightside	150	2.1×10^{27}	T21, T25, T26, T28, T29, T30, T32, T50, T55, T56, T57, T58, T59
Equatorial	145	2.1×10^{27}	T25, T26, T28, T37, T40, T43, T48, T55, T56, T57, T58, T61
Polar	153	3.1×10^{27}	T5, T16, T18, T19, T39, T49, T64
Sub-Saturn	152	2.3×10^{27}	T5, T23, T25, T26, T28, T29, T30, T32, T50, T64, T65, T71
Anti-Saturn	140	3.3×10^{27}	T16, T48, T49, T51, T55, T56, T57, T58, T59, T61
Ramside	157	2.0×10^{27}	T21
Wakeside	150	2.0×10^{27}	T18, T19, T36, T37, T39, T40, T41, T42, T43
Preequinox	153	2.3×10^{27}	all flybys up to T59
Postequinox	139	2.2×10^{27}	T61, T64, T65, T71
Plasma sheet	159	3.3×10^{27}	T5, T19, T23, T29, T36, T39, T49, T51, T55, T58
Lobe-like	115	DE	T18, T41, T43, T61
Bimodal	141	1.9×10^{27}	T26, T40
High proton flux	151	2.0×10^{27}	T18, T19, T21, T28, T32, T36, T39, T42, T50, T51, T56
Medium proton flux	151	1.9×10^{27}	T5, T23, T26, T29, T30, T37, T40, T49, T58, T59
Low proton flux	171	2.2×10^{27}	T25

^aAlso shown are the flybys included in each category. The diffusive equilibrium (DE) model provides reasonable description of the CH₄ data on the dayside and for lobe-like plasma conditions.

solar-driven model. Other features consistent with this include the nondetection of appreciable difference in CH₄ loss rate between the equatorial region and the polar region, or between preequinox and postequinox. Both meridional and seasonal trends might be present if CH₄ loss from Titan is primarily solar-driven, analogous to the findings of the variation of N₂/CH₄ densities and neutral temperature with latitude (MW08), as well as the decrease in altitude of the detached haze layer from before to after the equinox [West *et al.*, 2011].

[53] The above discussions motivate us to investigate the magnetospheric response of CH₄ escape on Titan. Ideally, varying plasma conditions are encountered for different zonal sectors. The actual situation is however more complicated, and a better categorization can be made in terms of the varying levels of electron precipitation in the 0.6 eV to 5 MeV range [Rymer *et al.*, 2009], ion precipitation in the 1 eV to 50 keV range [Németh *et al.*, 2011], or energetic proton precipitation in the 27–255 keV range [Garnier *et al.*, 2010]. Following these works, we list in Table 5 the characteristics of Titan's plasma environment for reference.

[54] Table 5 reveals that there is no systematic trend in CH₄ loss rate with longitude, and there is no evidence for elevated CH₄ escape with enhanced energetic proton precipitation or with the presence of enriched water group ions peaking at ~4400 eV [Németh *et al.*, 2011]. The latter is indicated by the *e* classification of bimodal in Table 5. However, we do identify a tentative trend with magnetospheric electron precipitation. This is illustrated in Figure 8 (fourth column), where we compare the INMS CH₄ mixing ratio profiles averaged over the plasma sheet and lobe-like categories with the respective diffusive equilibrium profiles. It is clear that strong CH₄ escape does occur for plasma sheet conditions, characterized by a relatively high peak electron flux of $\sim 3.5 \times 10^5$ to 1.2×10^6 cm⁻² s⁻¹ sr⁻¹ in the 120–600 eV energy range [Rymer *et al.*, 2009]. We note that among the six flybys in our sample that belong to this category, four show strong CH₄ escape on Titan. Especially, this category includes two of the three flybys with the largest CH₄ loss rates in Table 5. In contrast, for each of the two lobe-like flybys in our sample, the INMS CH₄ distribution is

reasonably described by diffusive equilibrium. According to Rymer *et al.* [2009], lobe-like conditions are characterized by an incident electron flux a factor of 10 lower than the plasma sheet value in a similar energy range. The magnetosheath category (not shown in Figure 8) also includes two flybys: one under diffusive equilibrium and the other one with a relatively low CH₄ loss rate of $\sim 1.5 \times 10^{27}$ s⁻¹. The incident electron flux for this category is comparable with the plasma sheet category but shifts to lower energies peaking at ~50 eV. Thus, if electron precipitation drives CH₄ escape on Titan, then the relevant electron energy range is more likely at the level of several hundred eV or above.

[55] In Table 6 we summarize the mean CH₄ loss rates for all categories that we consider above, along with the corresponding mean neutral temperatures. These are obtained from the isothermal and diffusion model fittings to the N₂ and CH₄ density profiles averaged over each category, rather than simply taking the averages over values in Table 5. The interpretation of the results in Table 6 deserves some caution. For most of the categories, the variations in CH₄ loss and neutral temperature are so large that comparisons between different categories do not lead to conclusive results. Thus, some of the tendencies revealed by Table 6, such as the preferential occurrence of strong CH₄ escape at the anti-Saturn side, are not statistically significant. The most rigorous conclusions that we can draw for the variability in CH₄ escape are probably the diurnal difference and the trend with varying electron precipitation, as the dayside and lobe-like categories are the only two cases in Table 6 with CH₄ distribution under diffusive equilibrium. The implications of these features have already been discussed above.

[56] The recent INMS investigation of Westlake *et al.* [2011] has revealed a trend of enhanced neutral temperature in Titan's upper atmosphere when exposed to elevated electron precipitation. Thus, CH₄ escape and neutral heating tend to occur under similar conditions. This may imply a potential correlation between the CH₄ loss rate and the neutral temperature, but the scattering of such a relation is quite large, as indicated in Figure 9. Indeed, Table 6 shows that a similar temperature is derived for both the dayside and

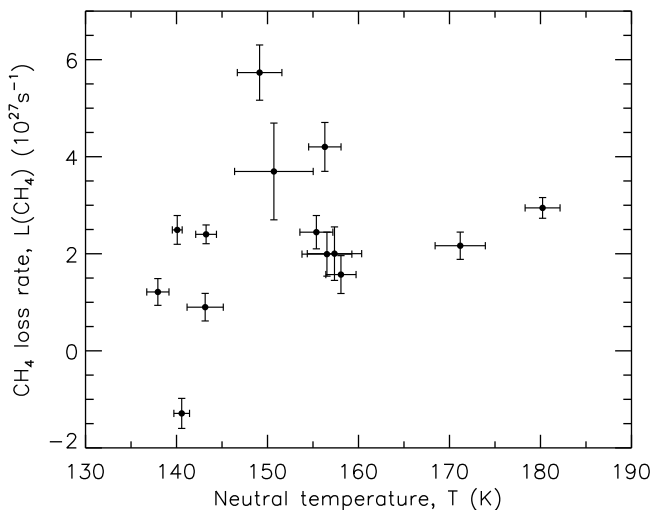


Figure 9. The CH₄ loss rate, $L(\text{CH}_4)$, as a function of the neutral temperature, T , for all flybys with strong CH₄ escape confirmed at $>3\sigma$ significance level (see text for details). No rigorous correlation can be identified between the two quantities.

nightside categories, but the CH₄ escape rates for the two categories are significantly different.

[57] At the face value, the variability in CH₄ escape revealed by Table 6 implies that CH₄ escape on Titan is more likely to be magnetospherically driven rather than solar driven. However, one important consideration complicates the above argument: In response to varying solar and/or magnetospheric conditions, the change in CH₄ distribution occurs within the diffusion timescale, $\tau_{\text{diff}} \sim H_i^2/D_i \approx 2$ h, where we have used a CH₄ scale height, H_i , of ~ 200 km and a CH₄ molecular diffusion coefficient, D_i , of $\sim 5 \times 10^{10}$ cm² s⁻¹ referred to 1400 km. For comparison, the timescale over which solar inputs vary, τ_{solar} , is about half a Titan day, i.e., $\tau_{\text{solar}} \approx 200$ h. This is significantly longer than τ_{diff} , ensuring that the solar response of CH₄ escape on Titan, if present, can in principle be observed in the INMS data. However, this is not necessarily the case for magnetospheric variations. *Simon et al.* [2010] have shown that on the nightside of Titan, the timescale for magnetic field variability could be as long as 5 h, whereas on the dayside, the timescale is typically 10^2 s. Thus, the timescale for magnetospheric variations is either comparable with or much shorter than τ_{diff} . For such cases, the time response of the CH₄ structure is not fast enough to leave an observable effect during a Titan encounter, and accordingly the apparent trend of CH₄ escape with magnetospheric electron precipitation may simply be a coincidence.

4. Concluding Remarks

[58] The inbound INMS data from 32 Cassini flybys with Titan are analyzed in this work, focusing on the CH₄ structure in the upper atmosphere of the satellite. Several updates in the data reduction algorithms have been implemented, including the improved treatment of the counter saturation characteristics, the removal of instantaneous transition in the N₂ and CH₄ density profiles, as well as the appropriate

decoupling between ⁴⁰Ar and other minor species. The analysis presented here is aimed at (1) solving the inconsistency in the interpretation of the CH₄ data between existing works [e.g., Y08; *Bell et al.*, 2011] and (2) investigating the variability of CH₄ escape among different flybys. Several questions raised in this paper are listed below along with our findings.

[59] 1. How important is eddy mixing on Titan? We use a diffusive equilibrium model to describe the ⁴⁰Ar mixing ratio profile, combining both the INMS data in the upper atmosphere and the GCMS data in the lower stratosphere [*Niemann et al.*, 2010]. The globally averaged asymptotic eddy mixing coefficient is $K_\infty \approx 2 \times 10^7$ cm² s⁻¹, based on the standard chemical model of *Strobel* [2012] as the input background atmosphere. The corresponding homopause level is at ~ 850 km, consistent with the early result of Y08 but in conflict with the 1000 km level suggested by *Bell et al.* [2011]. Over the altitude range probed by the INMS, molecular diffusion is significantly more important than eddy mixing. This has important impacts on the interpretation of the INMS CH₄ data.

[60] 2. Does strong CH₄ escape occur on Titan? With the current knowledge of eddy mixing (derived from the ⁴⁰Ar data) and neutral temperature (derived from the N₂ data), we conclude that strong CH₄ escape must occur on Titan. The nominal CH₄ loss rate is $\sim 3 \times 10^{27}$ s⁻¹ or 80 kg s⁻¹ in a globally averaged sense, in general agreement with the early results of Y08 and *Strobel* [2008, 2009]. The CH₄ loss rate is not a linear response of the ambient atmospheric parameters, as revealed by Figure 7. In practice, the CH₄ loss rate can only be reliably inferred when it is near or above the level of 10^{27} s⁻¹. This is fortunately the case for Titan's upper atmosphere, making it possible to constrain the globally averaged CH₄ loss rate with a diffusion model. The strong CH₄ escape implied by the INMS data makes only a small contribution to the CH₄ budget on Titan, with the bulk of the CH₄ molecules supplied from Titan's interior photochemically converted to more complex hydrocarbons [*Strobel*, 2009]. The main uncertainty in the derived globally averaged CH₄ loss rate is associated with the choice of the temperature profile. The possible range of CH₄ loss rate is $\sim (2.7\text{--}4.5) \times 10^{27}$ s⁻¹ in accord with the range of average temperature reported in existing works [e.g., Y08; C09; *Westlake et al.*, 2011].

[61] 3. How variable is CH₄ escape on Titan? *Cui et al.* [2011] have shown that the H₂ escape remains roughly stable from flyby to flyby, but the analysis in this work reveals a large variability of CH₄ escape on Titan. Specifically, about half of the flybys show evidences for strong CH₄ escape at the level of several 10^{27} s⁻¹, whereas for most of the other flybys, the CH₄ structures are reasonably described by diffusive equilibrium. This suggests that CH₄ escape on Titan is more likely a sporadic rather than a steady process. CH₄ inflow may also occur on Titan, though only occasionally. We search for systematic trends in CH₄ escape with varying solar and/or magnetospheric conditions. We find that strong CH₄ escape preferentially occurs on the nightside, in conflict with the expectations of any solar-driven model. However, no rigorous connection can be identified between the CH₄ loss rate and the precipitation of various magnetospheric species, except for an apparent trend of elevated CH₄ escape for plasma sheet conditions as compared to

lobe-like conditions. But this may simply be a coincidence as the time response of the CH₄ structure to magnetospheric inputs is not fast enough to leave an observable effect during a Titan encounter. The main uncertainties in the CH₄ loss rates derived for individual flybys are associated with the density fluctuations around the large-scale trends, presumably due to wave structures in the ambient atmosphere.

[62] In a more general context, how magnetospheric particle precipitation influences the structure of Titan's neutral atmosphere has recently drawn significant attention. This is a highly complicated and variable process, which may leave a variety of observational signatures. Elevated neutral temperature has been found to preferentially, but not always, occur under plasma sheet conditions [Westlake et al., 2011]. Thus, neutral heating and CH₄ escape may represent intermediate processes of a complex interaction between Titan's upper atmosphere and magnetosphere, if the enhanced CH₄ escape associated with plasma sheet (see section 3.3) is realistic. The relative importance of particle precipitation depends on the depth in the atmosphere, with different magnetospheric species depositing most of their energies at different altitude levels, either above or below where solar EUV/FUV radiation dominates [e.g., Michael and Johnson, 2005; Cravens et al., 2008; Smith et al., 2009]. The access of incident charged particles, especially electrons, into Titan's atmosphere is also strongly controlled by the ambient magnetic field configuration, which could be either a barrier or a gate [e.g., Galand et al., 2006; Ma et al., 2009; Richard et al., 2011]. Due to the above complexities, it is by no means possible to obtain any conclusive result based on a simple comparison between broad categories, as done in this work. Simulations of Titan's plasma-atmosphere interactions on a flyby-to-flyby basis and with realistic model inputs are required to eventually pin down the role of magnetospheric inputs on Titan's neutral atmosphere.

[63] **Acknowledgments.** J.C. acknowledges support from the National Science Foundation of China through grant NSFC-41174146. D.F.S. was supported by the Cassini-Huygens mission through JPL contract 1353551 and NASA grant NNG05G091G. I.M.W. acknowledges support from the UK Science and Technology Facilities Council (STFC).

References

- Bell, J. M., et al. (2010a), Simulating the one-dimensional structure of Titan's upper atmosphere: 2. Alternative scenarios for methane escape, *J. Geophys. Res.*, *115*, E12018, doi:10.1029/2010JE003638.
- Bell, J. M., et al. (2010b), Simulating the one-dimensional structure of Titan's upper atmosphere: 1. Formulation of the Titan Global Ionosphere-Thermosphere Model and benchmark simulations, *J. Geophys. Res.*, *115*, E12002, doi:10.1029/2010JE003636.
- Bell, J. M., et al. (2011), Simulating the one-dimensional structure of Titan's upper atmosphere: 3. Mechanisms determining methane escape, *J. Geophys. Res.*, *116*, E11002, doi:10.1029/2010JE003639.
- Bird, G. A. (1994), *Molecular Gas Dynamics and the Direct Simulation of Gas Flows*, pp. 2–3, Oxford Univ. Press, Oxford, U. K.
- Cravens, T. E., I. P. Robertson, S. A. Ledvina, D. Mitchell, S. M. Krimigis, and J. H. Waite Jr. (2008), Energetic ion precipitation at Titan, *Geophys. Res. Lett.*, *35*, L03103, doi:10.1029/2007GL032451.
- Cui, J., R. V. Yelle, and K. Volk (2008), Distribution and escape of molecular hydrogen in Titan's thermosphere and exosphere, *J. Geophys. Res.*, *113*, E10004, doi:10.1029/2007JE003032.
- Cui, J., et al. (2009), Analysis of Titan's neutral upper atmosphere from Cassini Ion Neutral Mass Spectrometer measurements, *Icarus*, *200*, 581–615, doi:10.1016/j.icarus.2008.12.005.
- Cui, J., R. V. Yelle, I. C. F. Müller-Wodarg, P. P. Lavvas, and M. Galand (2011), The implications of the H₂ variability in Titan's exosphere, *J. Geophys. Res.*, *116*, A11324, doi:10.1029/2011JA016808.
- De La Haye, V., et al. (2007), TitanUs corona: The contribution of exothermic chemistry, *Icarus*, *191*, 236–250, doi:10.1016/j.icarus.2007.04.031.
- Fulchignoni, M., et al. (2005), In situ measurements of the physical characteristics of Titan's environment, *Nature*, *438*, 785–791, doi:10.1038/nature04314.
- Galand, M., R. V. Yelle, A. J. Coates, H. Backes, and J.-E. Wahlund (2006), Electron temperature of Titan's sunlit ionosphere, *Geophys. Res. Lett.*, *33*, L21101, doi:10.1029/2006GL027488.
- Garnier, P., et al. (2010), Statistical analysis of the energetic ion and ENA data for the Titan environment, *Planet. Space Sci.*, *58*, 1811–1822, doi:10.1016/j.pss.2010.08.009.
- Koskinen, T. T., et al. (2011), The mesosphere and lower thermosphere of Titan revealed by Cassini/UVIS stellar occultations, *Icarus*, *216*, 507–534, doi:10.1016/j.icarus.2011.09.022.
- Lavvas, P. P., et al. (2011), Energy deposition and primary chemical products in Titan's upper atmosphere, *Icarus*, *213*, 233–251, doi:10.1016/j.icarus.2011.03.001.
- Ma, Y. J., et al. (2009), Time-dependent global MHD simulations of Cassini T32 flyby: From magnetosphere to magnetosheath, *J. Geophys. Res.*, *114*, A03204, doi:10.1029/2008JA013676.
- Magee, B. A., et al. (2009), INMS-derived composition of Titan's upper atmosphere: Analysis methods and model comparison, *Planet. Space Sci.*, *57*, 1895–1916, doi:10.1016/j.pss.2009.06.016.
- Michael, M., and R. E. Johnson (2005), Energy deposition of pickup ions and heating of Titan's atmosphere, *Planet. Space Sci.*, *53*, 1510–1514, doi:10.1016/j.pss.2005.08.001.
- Müller-Wodarg, I. C. F., and R. V. Yelle (2002), The effect of dynamics on the composition of Titan's upper atmosphere, *Geophys. Res. Lett.*, *29*(23), 2139, doi:10.1029/2002GL016100.
- Müller-Wodarg, I. C. F., R. V. Yelle, M. Mendillo, L. A. Young, and A. D. Aylward (2000), The thermosphere of Titan simulated by a global three-dimensional time-dependent model, *J. Geophys. Res.*, *105*, 20,833–20,856, doi:10.1029/2000JA000053.
- Müller-Wodarg, I. C. F., R. V. Yelle, N. Borggren, and J. H. Waite Jr. (2006), Waves and horizontal structures in Titan's thermosphere, *J. Geophys. Res.*, *111*, A12315, doi:10.1029/2006JA011961.
- Müller-Wodarg, I. C. F., R. V. Yelle, J. Cui, and J. H. Waite (2008), Horizontal structures and dynamics of Titan's thermosphere, *J. Geophys. Res.*, *113*, E10005, doi:10.1029/2007JE003033.
- Németh, Z., K. Szego, Z. Bebesi, G. Erdo's, L. Foldy, A. Rymer, E. C. Stittler, A. J. Coates, and A. Wellbrock (2011), Ion distributions of different Kronian plasma regions, *J. Geophys. Res.*, *116*, A09212, doi:10.1029/2011JA016585.
- Niemann, H. B., S. K. Atreya, J. E. Demick, D. Gautier, J. A. Haberman, D. N. Harpold, W. T. Kasprzak, J. I. Lunine, T. C. Owen, and F. Raulin (2010), Composition of Titan's lower atmosphere and simple surface volatiles as measured by the Cassini-Huygens probe gas chromatograph mass spectrometer experiment, *J. Geophys. Res.*, *115*, E12006, doi:10.1029/2010JE003659.
- Pang, T. (2006), *An Introduction to Computational Physics*, 2nd ed., pp. 285–320, Cambridge Univ. Press, Cambridge, U. K.
- Richard, M. S., T. E. Cravens, I. P. Robertson, J. H. Waite, J.-E. Wahlund, F. J. Crary, and A. J. Coates (2011), Energetics of Titan's ionosphere: Model comparisons with Cassini data, *J. Geophys. Res.*, *116*, A09310, doi:10.1029/2011JA016603.
- Rodrigo, R., E. García-Álvarez, M. J. López-González, and J. J. López-Moreno (1990), A nonsteady one-dimensional theoretical model of Mars' neutral atmospheric composition between 30 and 200 km, *J. Geophys. Res.*, *95*, 14,795–14,810, doi:10.1029/JB095iB09p14795.
- Rymer, A. M., H. T. Smith, A. Wellbrock, A. J. Coates, and D. T. Young (2009), Discrete classification and electron energy spectra of Titan's varied magnetospheric environment, *Geophys. Res. Lett.*, *36*, L15109, doi:10.1029/2009GL039427.
- Schäufelberger, A., P. Wurz, H. Lammer, and Y. N. Kulikov (2012), Is hydrodynamic escape from Titan possible?, *Planet. Space Sci.*, *61*, 79–84, doi:10.1016/j.pss.2011.03.011.
- Simon, S., A. Wennmacher, F. M. Neubauer, C. L. Bertucci, H. Kriegel, J. Saur, C. T. Russell, and M. K. Dougherty (2010), Titan's highly dynamic magnetic environment: A systematic survey of Cassini magnetometer observations from flybys TA-T62, *Planet. Space Sci.*, *58*, 1230–1251, doi:10.1016/j.pss.2010.04.021.
- Smith, H. T., D. G. Mitchell, R. E. Johnson, and C. P. Paranicas (2009), Investigation of energetic proton penetration in Titan's atmosphere using the Cassini INCA instrument, *Planet. Space Sci.*, *57*, 1538–1546, doi:10.1016/j.pss.2009.03.013.

- Strobel, D. F. (2008), Titan's hydrodynamically escaping atmosphere, *Icarus*, *193*, 588–594, doi:10.1016/j.icarus.2007.08.014.
- Strobel, D. F. (2009), Titan's hydrodynamically escaping atmosphere: Escape rates and the structure of the exobase region, *Icarus*, *202*, 632–641, doi:10.1016/j.icarus.2009.03.007.
- Strobel, D. F. (2010), Molecular hydrogen in Titan's atmosphere: Implications of the measured tropospheric and thermospheric mole fractions, *Icarus*, *208*, 878–886, doi:10.1016/j.icarus.2010.03.003.
- Strobel, D. F. (2012), Hydrogen and methane in Titan's atmosphere: Chemistry, diffusion, escape and the Hunten limiting flux principle, *Can. J. Phys.*, *90*, 795–805, doi:10.1139/p11-131.
- Tucker, O. J., and R. E. Johnson (2009), Thermally driven atmospheric escape: Monte Carlo simulations for Titan's atmosphere, *Planet. Space Sci.*, *57*, 1889–1894, doi:10.1016/j.pss.2009.06.003.
- Tucker, O. J., J. T. Erwin, J. I. Deighan, A. N. Volkov, and R. E. Johnson (2012), Thermally driven escape from Pluto's atmosphere: A combined fluid/kinetic model, *Icarus*, *217*, 408–415, doi:10.1016/j.icarus.2011.11.017.
- Volkov, A. N., R. E. Johnson, O. J. Tucker, and J. T. Erwin (2011), Thermally driven atmospheric escape: Transition from hydrodynamic to Jeans escape, *Astrophys. J. Lett.*, *729*, L24, doi:10.1088/2041-8205/729/2/L24.
- von Zahn, U., K. H. Fricke, H.-J. Hoffmann, and K. Pelka (1979), Venus: eddy coefficients in the thermosphere and the inferred helium content of the lower atmosphere, *Geophys. Res. Lett.*, *6*(5), 337–340, doi:10.1029/GL006i005p00337.
- Vuitton, V., R. V. Yelle, and J. Cui (2008), Formation and distribution of benzene on Titan, *J. Geophys. Res.*, *113*, E05007, doi:10.1029/2007JE002997.
- Waite, Jr., J. H., et al. (2004), The Cassini Ion and Neutral Mass Spectrometer (INMS) investigation, *Space Sci. Rev.*, *114*, 113–231, doi:10.1007/s11214-004-1408-2.
- West, R. A., J. Balloch, P. Dumont, P. Lavvas, R. Lorenz, P. Rannou, T. Ray, and E. P. Turtle (2011), The evolution of Titan's detached haze layer near equinox in 2009, *Geophys. Res. Lett.*, *38*, L06204, doi:10.1029/2011GL046843.
- Westlake, J. H., J. M. Bell, J. H. Waite Jr., R. E. Johnson, J. G. Luhmann, K. E. Mandt, B. A. Magee, and A. M. Rymer (2011), Titan's thermospheric response to various plasma environments, *J. Geophys. Res.*, *116*, A03318, doi:10.1029/2010JA016251.
- Yelle, R. V., N. Borggren, V. de la Haye, W. T. Kasprzak, H. B. Niemann, I. Müller-Wodarg, and J. H. Waite Jr. (2006), The vertical structure of Titan's upper atmosphere from Cassini Ion Neutral Mass Spectrometer measurements, *Icarus*, *182*, 567–576, doi:10.1016/j.icarus.2005.10.029.
- Yelle, R. V., J. Cui, and I. C. F. Müller-Wodarg (2008), Methane escape from Titan's atmosphere, *J. Geophys. Res.*, *113*, E10003, doi:10.1029/2007JE003031.